

Cetuximab-Conjugated Perfluorohexane/Gold Nanoparticles for Low Intensity Focused Ultrasound Diagnosis Ablation of Thyroid Cancer Treatment

Yue Ma

Harbin Medical University

Lingling Wang

Harbin Medical University

Haixia Li

Harbin Medical University

Wen Cheng

Harbin Medical University

Xiulan Zheng

Harbin Medical University

Ying Liu (✉ liuying865@yahoo.com)

Harbin Medical University <https://orcid.org/0000-0001-5106-650X>

Research

Keywords:

Posted Date: May 6th, 2020

DOI: <https://doi.org/10.21203/rs.3.rs-21316/v1>

License: © ⓘ This work is licensed under a Creative Commons Attribution 4.0 International License.

[Read Full License](#)

Version of Record: A version of this preprint was published at Science and Technology of Advanced Materials on January 31st, 2020. See the published version at

<https://doi.org/10.1080/14686996.2020.1855064>.

Abstract

Chemotherapeutic efficacy can be significantly developed nanotheranostics systems of drug delivery in tumor cells. In this work, we have demonstrated that the self-assembled by C225 conjugates Au-PFH-NPs (C-Au-PFH-NPs) for low intensity focused ultrasound diagnosis ablation of thyroid cancer treatment. C-Au-PFH-NPs have shown excellent stability in water, PBS and 20% rat serum. Transmission electron microscopy (TEM) images also exposed the effective construction of C-Au-PFH-NPs with commonly spherical sized assemblies. The incubation of the C625 thyroid carcinoma with C-Au-PFH-NPs triggers apoptosis, which was confirmed by the flowcytometry analysis. The C-Au-PFH-NPs, with remarkably displays the potent antitumor efficacy in a human thyroid carcinoma xenografts. A histopathological result reveals that precisely achieved to additional confirm these outcomes. Further, we successfully examined the efficiency of C-Au-PFH-NPs when used the thyroid carcinoma low intensity focused ultrasound diagnosis imaging (LIFUS) in vivo. These findings clearable for LIFUS agents with high performing image and different therapeutic purpose will have extensive possible for the future biomedical purposes.

1. Introduction

Anaplastic thyroid carcinoma (ATC) is one of the most malignant carcinomas, which is also comparatively rare, characterized by fast proliferation, neck invasion, and remote metastasis [1–4]. ATC's severe prognosis is due to the tumors' fast progression before diagnosis. Current treatment is based on different types of combinations in chemotherapy and exterior ray radiation has unsuccessful to enhance existence, resulting in an average existence rate of 4 to 6 months and less than 20% existence level in 12 months [5–8]. Here are therefore convincing explanations for developing a new theranostics approach for initial finding and efficient ATC treatment [9–11].

In a recent time, triggerable drug-charged nanocarriers coupled with multiple inner or external stimuli such as pH, temperature, ultrasound, laser, and microwave radiation have been extensively explored for personalized treatment to enable controlled release and have excellent possible to deliver an enhanced anticancer treatment impact also decreased systemic toxicity [12–14]. Low-intensity concentrated ultrasounds (LIFUS) have been exhaustively researched for tumour treatment and ultrasounds imaging analysis as one of the probable exterior activates which is non-invasive and displays significant tissue-penetrating capacity. In particular, it can significantly increase the efficacy of chemotherapy, avoiding harm to the nearby cells and reducing adversarial side effects [15]. Though, the discharge of LIFUS-triggered drugs from nanocarriers and further tumour therapy is still unsatisfactory, largely attributable to the comparatively less accumulation efficacy of nanoparticles-charged nano transporters at tumour places. There are numerous nanotransporters extensively examined on this basis to enhance the aggregation of large number of tumors without causing any side effects [15–17].

Several reports have shown that overexpression of the epidermal growth factor receptor (EGFR) is strongly associated with tumour progression, migration, and invasion. EGFR is common in ATC [18].

Antibodies or small molecules based on EGFR immunotherapy can significantly increase the therapeutic effect against ATC. A human murine chimeric EGFR-targeted monoclonal antibody called Cetuximab have higher empathy to human EGFR's extracellular domain and inhibits the signals of its epidermal growth factor in cells by delaying usual receptor function [19–21]. Food and Drug Administration approved preclinical and preclinical treatments using Cetuximab for the treatment of EGFR-expressing cancer tumors' neck and head carcinoma and colorectal carcinoma. This C225 might be a suitable objective for the nanocarriers' structure to improve the therapeutic outcome of ATCs. Remarkably, some researchers have revealed that for a wide spectrum of cancers, the blend of C225 with CPT-11 equivalents such as Au-PFH-NPs has significant synergetic antitumor effects [22–25]. Hence, Au-PFH-NPs in combination with C225 could enhance the ATC diagnostics. But, owing to less vascular dispersal of C225 and hydrophobicity of the Au-PFH-NPs, the NPs penetrability in the growth and the NPs quantity in the tumor area were inherently imperfect, shows greatly debilitated their anticancer efficacy. Opportunely, the problems can be enhanced through incorporating Au-PFH-NPs and C225 into a one nanotransporters to attain C225 and Au-PFH-NPs combination chemotherapy while simultaneously providing targeting capability for nanocarriers [26–29].

Furthermore, for early diagnosis and tumor progression monitoring medical imaging is essential. Numerous researchers proposed that LIFUS have the probable to achieve concurrent US and medication transfer, meeting the present need for initial treatment and ATC therapy [30–32]. Due to variability and huge dimensions of microbubbles to realize the tumor theranostic strategy conservative US agents, like as microbubbles, demonstration outstanding US agents for imaging capability but these not appropriate for drug delivery purposes. In order to avoid this problem, intensively studied phase-changing NPs that could be activated via LIFUS. The phase-changing NPs providing important benefits in tumor theranostics for the supply of tumor ultrasound and ultrasound-triggered drug [33–35]. This new strategy offers the possible to develop malignancy treatment and addresses the present theranostic needs in contradiction of ATC significantly.

The objective of this work was to constructed the modification of C225 nanocarrier to exactly prevent ATC that might accrue in cancer cells, in addition to the EPR effect, through the great tumor homing belongings of C225. The Au-PFH-NPs payload could be released and LIFUS-triggered synergistic chemotherapy with C225 may perhaps suggestively make best use of therapeutic efficacy, improve USI and diminish the side effects of chemotherapy. As shown in Fig. 1. Due to its tremendous biodegradability and biocompatibility, we used a PHF (Perfluorohexane) core as the shell structure of the nanocarrier. We then synthesized phase-changing NPs with Perfluorohexane liquid (PHF, 29 °C boiling point). Meanwhile, Au-PFH-NPs were burdened into the nanoparticles at the similar period of time as C225 was conjugated on surface of gold nanoparticles afford (C-Au-PFH-NPs) C225-conjugated Au-PFH-NPs-charged phase transformation. To our knowledge, this is the first work of a LIFUS-mediated C225 modified nanosyste that assimilates tumor targeted both US imagery and US activated drug conveyance to ATC.

2. Experimental Section

The detailed experimental procedures are given in the supporting information.

2.1. Cell culture and nude mice

The Cell Bank of the Chinese Academy of Sciences (Shanghai, China) acquired a human anaplastic thyroid carcinoma line (C643). The cells were grown in medium RPMI-1640 containing 10% FBS and 1% penicillin-streptomycin at 37 °C in humidified air with 5% CO₂. At the Laboratory Animal Center of Department of Ultrasound, Harbin Medical University Cancer Hospital (Harbin, China), BALB/C Female both mice and nude mice (balancing about 19 g, 25 days) were bought then raised. All animals on our studies were collected from the Harbin Medical University Cancer Hospital Laboratory Animal Center and retained in accordance with rules authorized by the Harbin Medical University's Animal Ethics Committee (Harbin, China). Furthermore, all animal experimental activities were strictly in line with the policy of the Harbin Medical University's Institutional Animal Care and Use Committee (IACUC), and this study was endorsed by the IACUC.

In order to start an ATC model in nude mice, C643 cells were collected, splashed thrice with the FBS free medium of RPMI-1640, and subcutaneously inoculated into each mouse's left flank (3×10^7 C643 cells in 150 μ L FBS free medium of RPMI-1640 each mice). A Vernier caliper was used to measure the length and width of the tumour and the tumour quantity was considered by the calculation: volume-(length as width \times 2)/2.

2.2. *In vitro* analysis

2.2.1. In vitro intracellular uptake C-Au-PFH-NPs

In cultivation dishes, seeded the C643 cells for CLSM at a mass of 1×10^6 cell mL/dish, grown at 37 °C in moistened air comprising 5% CO₂. The cells were spilt into four groups after 24 h of culture: C-Au-PFH-NPs were handled respectively with 10 min and 15 min DiI- labeled C-Au-PFH-NPs (1 mg/mL), and after blocking the cells were washed three times with PBS. Then, DiI- labeled C-Au-PFH-NPs (1 mg/mL) incubated the cells. The cells were washed with PBS three times after 2 h incubation with nanoparticles, fixed with 4 percent paraformaldehyde (200 μ L) for 15 minutes, and then gestated by DAPI (10 μ g/mL, 200 μ L) for 20 min. Lastly, CLSM pictured the dishes [36–38].

2.2.3. In vitro cytotoxicity assay

The CCK-8 assay assessed the cell viability. C643 cells were seeded into 96-well plates (1×10^3 cells per well, 100 μ L). After 24- hours' incubation to assess the cell viability Au-PFH-NPs and C-Au-PFH-NPs treated at levels of 10, 5, 2.5, 1.25, 0.625 and 0.312 μ M for 24 hours. Au-PFH-NPs and C-Au-PFH-NPs cells were

incubated for 24 hours. The positive control used as the untreated C643 cells. The *in vitro* cytotoxicity assay performed and the calculated made by the company manufactures guidelines.

2.2.4. Apoptosis examinations

The cells were seeded (4×10^6 C643 cells per well, 1.5 mL) into a 6-well dish and grown at 37 °C in a humidified incubator with 5% CO₂ for 24 hours. The IC₅₀ concentration used by Au-PFH-NPs and C-Au-PFH-NPs. The cell apoptosis assay grouping technique was in accordance with the cell viability assay group. After administering IC₅₀ concentration of the formulations of Au-PFH-NPs and C-Au-PFH-NPs was implemented 2 hours later [39–41].

2.2.5. Cell cycle arrest examinations

The cells were seeded (4×10^6 C643 cells per well, 1.5 mL) into a 6-well dish and grown at 37 °C in a humidified incubator with 5% CO₂ for 24 hours. The IC₅₀ concentration used by Au-PFH-NPs and C-Au-PFH-NPs. The cells were gathered and analyzed in the PI-stained cells after 24 hours of culture, and the percentages of the cells in the G0/G1, S phase, and G2/M phases were evaluated [42–44].

2.2.6. *In vitro* fluorescence imaging in xenografts tumour

A continuous dosage of DiR labeled Au-PFH-NPs and C-Au-PFH-NPs (2 mg/mL, 200µL) was given to C643 tumour-bearing mice. With 1% pentobarbital, all mice were totally narcotized and fluorescence pictures were acquired before injection and 3 h, 6 h and 24 h post-injection. A vivid fluorescence imaging for tiny animals evaluated the fluorescence intensity changes in the tumour areas *in vivo*. For *ex vivo* fluorescence imaging, the significant organs and tumour of one mouse were gathered. In addition, Dil-labeled Au-PFH-NPs and C-Au-PFH-NPs (2.5 mg per mL, 150 µL) were injected through the intravenous of C643 tumour-bearing mice were injected six hours after injection. At the predetermined post-injection moment, tumour matters and significant tissues were gathered, segmented, and ice-covered. DAPI dyeing was conducted in the dark for 5 min after fastening with 4% paraformaldehyde. The biodistribution of Dil-labeled Au-PFH-NPs and C-Au-PFH-NPs was monitored by CLSM [45–47].

2.2.7. Therapeutic efficacy of *in vivo*

When the subcutaneous tumour reaches 100 mm³ in volume, an antitumour assay was conducted on xenografts of mice carrying anaplastic thyroid cancer. The tumour-bearing mice were arbitrarily split into 3 communities (n-5 per unit): control group (Saline) and free Au-PFH-NPs and C-Au-PFH-NPs were administered by the organizations. Two hundred microliters of the blend was injected with the same dose of Au-PFH-NPs and C-Au-PFH-NPs (1 mg/kg) through the tail vein in a 1% saline solution were determined six hours after injection with the US agent filling the investigation with the tumour superficial. Afterward the inoculations of C643 cells, 5 consecutive treatments were performed each 72 hours starting on day 20 and ending on day 37. Each mouse's tumour dimensions and weight was recovered every three days, and changes in tumour volume were examined from the relative tumour dimensions V/V_0 (V_0 : initial volume prior to treatment), and tumour growth curves were drawn at the same time. On day 37 days, all mice were euthanized and dissected and weighed the tumour masses. In addition, studies in histology

and immunohistochemistry were conducted. Sections of the tissue were stained with histopathology [48–50].

3. Results And Discussion

3.1. C-Au-PFH-NPs characterization

3.1. Description of C-Au-PFH-NPs

Having these both compounds in hand, we have examined the TEM analysis of Au-PFH-NPs (1 and 1a zoom view) and C-Au-PFH-NPs (Figs. 1 and 2). we next tested whether they are able to recapitulate self-assembly behavior in aqueous solutions. For this purpose, we dissolved the C-Au-PFH-NPs prodrugs in DMSO (10 mg/mL) and then rapidly injected them into deionized (DI) water under ultrasonication. This procedure allows us to validate the solution was found to be transparent and slightly bluish. Observation by electron microscopy revealed that the drug molecules self-assembled to form a spherical nanoparticle structure. DLS showed a single peak distribution of the nanoparticles. The average hydrodynamic diameter (intensity) of the compound 1 was about 107.1 nm, and the compound 2 was about 108.0 nm (Fig. 2B). However, there is a certain adhesion between the nanoparticles formed by the self-assembly of simple small molecule drugs [51–53]. Therefore, we have miscible with many hydrophobic drugs by combining the prodrug with the appropriate amount of C225 molecules. These nano-assemblies are formed and have been widely used for in vivo drug delivery, aiming to solve the problem of adhesion and to optimize cancer-specific drug delivery. Then, we measured the stability of C-Au-PFH-NPs with various parameters such as water, PBS and 20% rat serum which shows significantly stable size in various parameters (Fig. 2C). Taken together, although C-Au-PFH-NPs can self-assemble to form nanoparticles, they may not be stable enough. Therefore, C225 nanoparticles loaded with Au-PFH were investigated further to evaluate anticancer efficacy in vitro.

3.3. *In vitro* cell experiments

3.3.1. *In vitro* intracellular uptake

As illustrated in Fig. 3, the much tougher red fluorescence derived from Dil-labeled C-Au-PFH-NPs was additional obviously concentrated in the C-Au-PFH-NPs group around the cytomembrane of C643 cells compared to the non- target and antagonistic groups [54]. Furthermore, bigger quantities of red fluorescence were noted after exposure to C-Au-PFH-NPs group. These findings stated that through the elevated tumour -homing characteristics of C225, C-Au-PFH-NPs could fix tightly to C643 cells, and considerably encouraged intracellular uptake by the C643 cells. In the resentment group, C-Au-PFH-NPs lost the capacity to objective the C643 cells because the congested by surplus free C225, leading in small levels of C-Au-PFH-NPs around the cells and demonstrating that C-Au-PFH-NPs desired targeting effectiveness was the outcome of the EGFR- mediated directing capacity.

3.3.2. *In vitro* cytotoxicity assay

The CCK-8 assay assessed the cell viability of different NP formulations at distinct levels, showing a dose dependent model. As illustrated in Fig. 4A, the cell viability of nanoparticles in the analyzed dose range was noted at more than 80%, level at 10 mg per mL. The comparatively small insignificant viability proposed that the elevated biocompatibility of phase-changing nanoparticles was appropriate aimed at in vivo application. Reasonably, Au-PFH-NPs and C-Au-PFH-NPs cell viabilities decreased considerably as levels of C-Au-PFH-NPs also increased. In particular, the cell viability of the cells treated with C-Au-PFH-NPs was the low at the same concentration, implying that the mixture of C-Au-PFH-NPs could boost cytotoxicity synergistically. The cell viability of C-Au-PFH-NPs. The remarkably improved cytotoxicity of C-Au-PFH-NPs may lead from the increased

cell membrane permeability caused by the cavitation effect and the improved C-Au-PFH-NPs at the objective place, which significantly increased the inhibitory impression of C-Au-PFH-NPs on cell development.

3.3.3. Cell apoptosis and cell cycle assay

Next, the evaluation of cellular apoptosis. In several groups, total apoptosis (TA) improved as follows: control and respectively Au-PFH-NPs and C-Au-PFH-NPs (Fig. 4B). It should be noted that the apoptosis proportion of Au-PFH-NPs was smaller than that of C-Au-PFH-NPs, whereas it was significantly greater than that of C-Au-PFH-NPs. Cell cycle assays were also carried out to evaluate whether the cell cycle was influenced by the anti-proliferation used by Au-PFH-NPs and C-Au-PFH-NPs. A higher percentage of the G2/M phase was perceived in all preserved sets compared to the control group (Fig. 4C). The arrest cycle in the C-Au-PFH-NPs G2/M phase was higher than that in the control group but higher than that in the C-Au-PFH-NPs, which is consistent with the outcomes of cytotoxicity and apoptosis assays mentioned above. Hence, we detected an enhanced proportion of the cell cycle in the G2/M phase and the distinct declaration stages can be ascribed to the distinct effects among distinct tumour cells. Hence, C-Au-PFH-NPs showed important cell cycle arrest in C643 cells during the G2/M phase impact.

Complete deliberation of the outcomes of the in vitro experiment obviously stated that nanoparticles could aid as an exceptional vehicle for Au-PFH-NPs and C-Au-PFH-NPs, and the combination of C225 enabled the target to enhance cell recognition and endocytosis and enhance the therapeutic effect of C-Au-PFH-NPs. Furthermore, maximizing the cell proliferation inhibitory impacts. It may lead from the increased cell membrane permeability caused by cavitation and UTMD effects improved release of C-Au-PFH-NPs at the objective site, which significantly increased the inhibitory effect on proliferation of the tumor cells.

3.4. *In vivo* fluorescence imaging in xenografts tumour

In order to assess the targeting effectiveness and biodistribution of Au-PFH-NPs and C-Au-PFH-NPs *in vitro*, fluorescence imaging was implemented at prearranged period opinions. Compared to the non-targeted group's small fluorescence signal at each stage in time, the targeted group's important accumulating fluorescence signal seemed at the tumour place and peaky at 6 hours at values 6 fold greater than control group (3.94 ± 0.98) sometimes 109 vs. (9.03 ± 1.02), respectively, $108 \text{ (ps/cm}^{-2}\text{/sr)}/(\mu\text{W/cm})$ (Fig. 5A). The intensity of the fluorescence removed tumour and significant tissues were examined after 24 h *ex vivo*, and the tumour intensity fluorescence in the selected group was still 2 fold greater than that in the non-target group (2.99 ± 0.38) sometimes 108 vs. (2.09 ± 0.32), respectively, $108 \text{ (ps/cm}^{-2}\text{/sr)}/(\mu\text{W/cm})$. There was virtually no distinction between the targeted and non-targeted groups in the fluorescence intensified in the significant bodies. Meanwhile, considerably greater fluorescence red signals were noted in the targeted group's tumour cryosections at 6 hours under CLSM following tumour tissue ultrathin segmenting relative to the less signals red in the non-target group. The aforementioned should be noted that in the tumour cryosections of the Au-PFH-NPs group the red fluorescence signals were significantly improved compared to that of the C-Au-PFH-NPs group after irradiation. The distribution of the fluorescence signal in the main organs showed no important alteration in both group but primarily in the liver and spleen (Fig. 5B and C). The nontargeted group's low fluorescence signals at the tumour place may outcome from the EPR effect, which facilitated inert combination in tumour tissues, whereas the targeted group's greater fluorescence signal was primarily due to the C225-mediated endocytosis mechanism. In addition, C-Au-PFH-NPs could overcome tumour biological barriers, and the accumulation of C-Au-PFH-NPs at the objective places was endorsed after microbubble oscillation, cavitation and destruction. During the

process of the oscillation and crash of the acoustic microbubble by the US targeted microbubble removal impact, the cell membrane could be interrupted and the permeability enhanced, allowing more effective accumulation of C-Au-PFH-NPs at the objective locations. These conclusions more confirmed that C225 might precisely effort nanocarriers to tumour cells, preventing them from rapidly re-entry into systemic circulation and this allowing extra vascular diagnosis and efficient antitumour therapy with an agent.

3.3.7. *In vitro* ultrasound imaging

Based on Au-PFH-NPs and C-Au-PFH-NPs targeted accumulation capacity in tumour cells, we gambled that the phase changing nanoparticles can aid as US contrast to improve USI and treatment scratches [55–57]. Following the administration of various medicines before LIFUS irradiation, even less or anechoic and less contrast improved US signals were noted in each groups (Fig. 6A). Six hours after the administration of various treatments, LIFUS was performed in all groups same time periods with *in vivo* ultrasound imaging. In comparison with the saline, expressively sturdier spot like echo signs slowly accrued in both modes at the tumour places in the treated group, while no evident deviations were detected in the saline group, and only negligible signs looked in the non-target group. This outcome recommended that C225 eased the directing of tumour tissue accretion, and huge quantities of microbubbles were produced when phase-changing NPs were subjected to ADV at the LIFUS triggered tumour site, resultant in improved US imaging. Though, owing to the absence of C225-mediated targeting capacity, the Au-PFH-NPs and C-Au-PFH-NPs inadequate ADV could not effectively improve ultrasound imaging. Furthermore, apparent enrichment without LIFUS irradiation was not found in the Au-PFH-NPs and C-Au-PFH-NPs alone could not *in vitro* improve the ultrasound imaging shown in Fig. 6B-D. These findings showed that because of their relative stability, C-Au-PFH-NPs were appropriate as ultrasound imaging agents and efficient *in vivo* nanocarriers. The above

information were compatible with the outcomes of ultrasonic imaging, additional checking the effectiveness of the beleaguered ultrasonic of C-Au-PFH-NPs lower than LIFUS irradiation and local LIFUS radioactivity can boost the precision of phase changing C-Au-PFH-NPs.

3.3.8. Therapeutic efficacy of *in vivo*

The antitumour efficacy *in vivo* was explored in subcutaneous C643 models, interested by the notable therapeutic efficacy of the mixture of Au-PFH-NPs and C-Au-PFH-NPs *in vitro*. In order to demonstrate the therapy impact, numerical pictures of separate groups of mice was drawn. (Fig. 7A-C). The therapeutic effectiveness was evaluated by tracking changes in each group's tumour volume. The tumour in the saline groups the debauched and there was no significant decrease in the tumour dimensions in the C-Au-PFH-NPs group, indicating that the dose of C-Au-PFH-NPs was dependable *in vivo* and the well-known epidermal growth factor is target for tumour cell identification and treatment. But, C-Au-PFH-NPs accumulation at the tumour site depended solely on the existence of vessel fenestrations and vascular leakage, and inadequate drug release from the tumour site restricted the therapeutic effect. These findings showed that C-Au-PFH-NPs in nude mice could additional enhance the therapeutic effect of anaplastic subcutaneous thyroid cancer. Simultaneously, compared with control (saline) groups, H&E, procaspase 9 (brown), cleaved-caspase 3 (brown) expression levels are enhanced. Then, the Ki67 staining and TUNEL assay were showed to measure the apoptosis of the tumor *in vivo* (Fig. 7D) Furthermore, during the course of therapy, C-Au-PFH-NPs show no statistically important distinction in body weight between all mice groups. But, Au-PFH-NPs significantly reduce body weight.

The above findings obviously showed that in nude mice, the combination of C-Au-PFH-NPs attained a notable excellent therapeutic effect counter to ATC, importance the security of

beleaguered tumour treatment. This diagnostic approach is a preferred method for ATC of the thyroid, significantly improving the healing capacity lacking noticeable side effects.

4. Conclusion

The data offered here highpoint a strategy rationale for concurrently attractive the effectiveness and safety of extremely Au-PFA-NPs. As the synthetic Au-PFA-NPs and C-Au-PFA-NPs are fully biocompatible composites with minimal modifications, the safety risks can be minimized when considering their clinical translation. Furthermore, given the ability of Au-PFA-NPs to overcome the Cetuximab (C225)-Conjugated C-Au-PFA-NPs, it was expected that our approach could have high value as an optional therapeutic platform to treat patients with drug-resistant cancer. Lastly, we envision that in addition to taxane agents, this C-Au-PFA-NPs -based approach could be a simple yet broadly applicable strategy to make improved tolerated and more well-organized cytotoxic nanotherapeutics from other antitumor agents.

Declarations

Acknowledgements

None

Authors' contributions

Y.M. and L.W. assisted with NP synthesis and characterization; H. L. assisted with molecular and biochemical analysis; W.C. and X.Z. - assisted with data curation, formal analysis, and validation; Y.L. assisted with supervised the research.

Funding

None

Availability of data and materials

All data and material are included in the article and its additional files.

Ethics approval and consent to participate

All animal experiments were approved by the Ethics Committee of the Harbin Medical University Cancer Hospital in accordance with the guidelines on animal care and use (File No: 2018-3).

Consent for publication

Not applicable.

Competing interests

The authors declare that they have no competing interests.

References

1. Valkenborgh C, Médart L, Collignon L. Muscle Metastasis from Undifferentiated (Anaplastic) Thyroid Carcinoma. *Journal of the Belgian Society of Radiology*. 2019;103:27. doi:10.5334/jbsr.1604.
2. 10.1530/EDM-19-0085
Yamazaki H, Iwasaki H, Suganuma N, Toda S, Masudo K, Nakayama H, Rino Y, Masuda M, Anaplastic thyroid carcinoma diagnosed after treatment of lenvatinib for papillary thyroid carcinoma, *Endocrinology, Diabetes & Metabolism Case Reports*. 2019 (2019). doi:10.1530/EDM-19-0085.
3. Shelly D, Gupta D, Mishra S, Bharadwaj R. Osteoclastic variant of anaplastic thyroid carcinoma: A case report of rare entity. *Journal of Cancer Research Therapeutics*. 2019;15:704–7. doi:10.4103/jcrt.jcrt_355_16.
4. Spartalis E, Athanasiadis DI, Chrysikos D, Spartalis M, Boutzios G, Schizas D, Garpis N, Damaskos C, Paschou SA, Ioannidis A, Tsourouflis G, Dimitroulis D, Nikiteas NI. Histone Deacetylase Inhibitors and Anaplastic Thyroid Carcinoma, *Anticancer Research*. 39 (2019) 1119–1127. doi:10.21873/anticancer.13220.
5. Gou L, Zou H, Li B. Long noncoding RNA MALAT1 knockdown inhibits progression of anaplastic thyroid carcinoma by regulating miR-200a-3p/FOXA1. *Cancer Biology Therapy*. 2019;20:1355–65. doi:10.1080/15384047.2019.1617567.
6. Kim J-Y, Youn HY, Choi J, Baek SK, Kwon SY, Eun BK, Park J-Y, Oh KH. Anoctamin-1 affects the migration and invasion of anaplastic thyroid carcinoma cells. *Animal Cells Systems*. 2019;23:294–301. doi:10.1080/19768354.2019.1614981.
7. 10.1155/2019/9734576
Pan Z, Li L, Fang Q, Qian Y, Zhang Y, Zhu J, Ge M, Huang P, Integrated Bioinformatics Analysis of Master Regulators in Anaplastic Thyroid Carcinoma, *BioMed Research International*. 2019 (2019) 9734576. doi:10.1155/2019/9734576.
8. Eshraghi R, Barkan GA, Pambuccian SE. Rhabdoid cells in the fine needle aspirate of a neck mass in a patient with history of melanoma: Anaplastic thyroid carcinoma. *Diagnostic Cytopathology*. 2019;47:1232–6. doi:10.1002/dc.24284.
9. Jiao C, Li L, Zhang P, Zhang L, Li K, Fang R, Yuan L, Shi K, Pan L, Guo Q, Gao X, Chen G, Xu S, Wang Q, Zuo D, Wu W, Qiao S, Wang X, Moses R, Xiao J, Li L, Dang Y, Li X. REGy ablation impedes dedifferentiation of anaplastic thyroid carcinoma and accentuates radio-therapeutic response by regulating the Smad7-TGF- β pathway. *Cell Death Differ*. 2019. doi:10.1038/s41418-019-0367-9.
10. Chavez AAL, Iyer P, Cazacu IM, Cabanillas ME, Rashid A, Bhutani MS. Anaplastic Thyroid Carcinoma with Gastric Metastasis. *Current Health Sciences Journal*. 2018;44:294–8. doi:10.12865/CHSJ.44.03.14.

11. Li Z, Zhang Y, Wang R, Zou K, Zou L. Genetic alterations in anaplastic thyroid carcinoma and targeted therapies. *Experimental Therapeutic Medicine*. 2019;18:2369–77. doi:10.3892/etm.2019.7869.
12. Fomenko A, Lozano AM. Neuromodulation and ablation with focused ultrasound - toward the future of noninvasive brain therapy. *Neural Regeneration Research*. 2019;14:1509–10. doi:10.4103/1673-5374.255961.
13. Lemaire T, Neufeld E, Kuster N, Micera S. Understanding ultrasound neuromodulation using a computationally efficient and interpretable model of intramembrane cavitation. *Journal of Neural Engineering*. 2019;16:46007. doi:10.1088/1741-2552/ab1685.
14. Liu Z, Ran H, Wang Z, Zhou S, Wang Y. Targeted and pH-facilitated theranostic of orthotopic gastric cancer via phase-transformation doxorubicin-encapsulated nanoparticles enhanced by low-intensity focused ultrasound (LIFU) with reduced side effect. *International Journal of Nanomedicine*. 2019;14:7627–42. doi:10.2147/IJN.S212888.
15. Fomenko A, Neudorfer C, Dallapiazza RF, Kalia SK, Lozano AM. Low-intensity ultrasound neuromodulation: An overview of mechanisms and emerging human applications. *Brain Stimulation*. 2018;11:1209–17. doi:10.1016/j.brs.2018.08.013.
16. Schindler K, Wiest R, Kollar M, Donati F. EEG analysis with simulated neuronal cell models helps to detect pre-seizure changes, *Clinical Neurophysiology*. Official Journal of the International Federation of Clinical Neurophysiology. 2002;113:604–14. doi:10.1016/s1388-2457(02)00032-9.
17. Schindler K, Wiest R, Kollar M, Donati F. Using simulated neuronal cell models for detection of epileptic seizures in foramen ovale and scalp EEG, *Clinical Neurophysiology: Official Journal of the International Federation of Clinical Neurophysiology*. 112 (2001) 1006–1017. doi:10.1016/s1388-2457(01)00522-3.
18. Simões-Pereira J, Capitão R, Limbert E, Leite V. Anaplastic Thyroid Cancer: Clinical Picture of the Last Two Decades at a Single Oncology Referral Centre and Novel Therapeutic Options, *Cancers*. 11 (2019). doi:10.3390/cancers11081188.
19. Ljubas J, Ovesen T, Rusan M. A Systematic Review of Phase II Targeted Therapy Clinical Trials in Anaplastic Thyroid Cancer, *Cancers*. 11 (2019). doi:10.3390/cancers11070943.
20. Jin J, Wu X, Yin J, Li M, Shen J, Li J, Zhao Y, Zhao Q, Wu J, Wen Q, Cho CH, Yi T, Xiao Z, Qu L. Identification of Genetic Mutations in Cancer: Challenge and Opportunity in the New Era of Targeted Therapy. *Frontiers in Oncology*. 2019;9:263. doi:10.3389/fonc.2019.00263.
21. Garcia C, Buffet C, El Khattabi L, Rizk-Rabin M, Perlemoine K, Ragazzon B, Bertherat J, Cormier F, Groussin L. MET overexpression and activation favors invasiveness in a model of anaplastic thyroid cancer. *Oncotarget*. 2019;10:2320–34. doi:10.18632/oncotarget.26798.
22. 10.1155/2019/3017360
Qiu W, Zhang C, Wang S, Yu X, Wang Q, Zeng D, Du P, Ma J, Zheng Y, Pang B, Yu Y, Long F, Pang X, Sun Z, A Novel Anti-EGFR mAb Ame55 with Lower Toxicity and Better Efficacy than Cetuximab When

- Combined with Irinotecan, *Journal of Immunology Research*. 2019 (2019) 3017360. doi:10.1155/2019/3017360.
23. Zhu Y, Li J, Jing F, Ji T, Guo X, Yang J, Jiao S. Evaluation of the immune factors in the tumor environment before and after the treatment of cetuximab combined with chemotherapy. *World Journal of Surgical Oncology*. 2013;11:226. doi:10.1186/1477-7819-11-226.
 24. Cáceres B, Ramirez A, Carrillo E, Jimenez G, Griñán-Lisón C, López-Ruiz E, Jiménez-Martínez Y, Marchal JA, Boulaiz H. Deciphering the Mechanism of Action Involved in Enhanced Suicide Gene Colon Cancer Cell Killer Effect Mediated by Gef and Apoptin, *Cancers* 11 (2019). doi:10.3390/cancers11020264.
 25. Boyle KE, Patinkin ZW, Shapiro ALB, Bader C, Vanderlinden L, Kechris K, Janssen RC, Ford RJ, Smith BK, Steinberg GR, Davidson EJ, Yang IV, Dabelea D, Friedman JE. Maternal obesity alters fatty acid oxidation, AMPK activity, and associated DNA methylation in mesenchymal stem cells from human infants. *Molecular Metabolism*. 2017;6:1503–16. doi:10.1016/j.molmet.2017.08.012.
 26. Wang F, Porter M, Konstantopoulos A, Zhang P, Cui H. Preclinical development of drug delivery systems for paclitaxel-based cancer chemotherapy. *Journal of Controlled Release: Official Journal of the Controlled Release Society*. 2017;267:100–18. doi:10.1016/j.jconrel.2017.09.026.
 27. Prewett MC, Hooper AT, Bassi R, Ellis LM, Waksal HW, Hicklin DJ. Enhanced antitumor activity of anti-epidermal growth factor receptor monoclonal antibody IMC-C225 in combination with irinotecan (CPT-11) against human colorectal tumor xenografts, *Clinical Cancer Research: An Official Journal of the American Association for Cancer Research*. 8 (2002) 994–1003. <http://europepmc.org/abstract/MED/12006511>.
 28. Zaidman NA, Panoskaltsis-Mortari A, O'Grady SM. Differentiation of human bronchial epithelial cells: role of hydrocortisone in development of ion transport pathways involved in mucociliary clearance. *American Journal of Physiology Cell Physiology*. 2016;311:C225-36. doi:10.1152/ajpcell.00073.2016.
 29. Huang C-Q, Min Y, Wang S-Y, Yang X-J, Liu Y, Xiong B, Yonemura Y, Li Y. Cytoreductive surgery plus hyperthermic intraperitoneal chemotherapy improves survival for peritoneal carcinomatosis from colorectal cancer: a systematic review and meta-analysis of current evidence. *Oncotarget*. 2017;8:55657–83. doi:10.18632/oncotarget.17497.
 30. Ishihara S, Onoda N, Noda S, Asano Y, Tauchi Y, Morisaki T, Kashiwagi S, Takashima T, Ohira M. Sorafenib inhibits vascular endothelial cell proliferation stimulated by anaplastic thyroid cancer cells regardless of BRAF mutation status. *International Journal of Oncology*. 2019;55:1069–76. doi:10.3892/ijo.2019.4881.
 31. Wang JR, Zafereo ME, Dadu R, Ferrarotto R, Busaidy NL, Lu C, Ahmed S, Gule-Monroe MK, Williams MD, Sturgis EM, Goepfert RP, Gross ND, Lai SY, Gunn GB, Phan J, Rosenthal DI, Fuller CD, Morrison WH, Iyer P, Cabanillas ME. Complete Surgical Resection Following Neoadjuvant Dabrafenib Plus Trametinib in BRAFV600E-Mutated Anaplastic Thyroid Carcinoma, *Thyroid. Official Journal of the American Thyroid Association*. 2019;29:1036–43. doi:10.1089/thy.2019.0133.

32. 10.1155/2019/8218949
Corrigan KL, Williamson H, Elliott Range D, Niedzwiecki D, Brizel DM, Mowery YM, Treatment Outcomes in Anaplastic Thyroid Cancer, *Journal of Thyroid Research*. 2019 (2019) 8218949. doi:10.1155/2019/8218949.
33. Bi JW, Zou YL, Qian JT, Chen WB. MiR-599 serves a suppressive role in anaplastic thyroid cancer by activating the T-cell intracellular antigen. *Experimental Therapeutic Medicine*. 2019;18:2413–20. doi:10.3892/etm.2019.7864.
34. Wu X, Benov A, Darlington DN, Keese JD, Liu B, Cap AP. Effect of tranexamic acid administration on acute traumatic coagulopathy in rats with polytrauma and hemorrhage. *PloS One*. 2019;14:e0223406. doi:10.1371/journal.pone.0223406.
35. McGonagle ER, Nucera C. Clonal Reconstruction of Thyroid Cancer: An Essential Strategy for Preventing Resistance to Ultra-Precision Therapy. *Frontiers in Endocrinology*. 2019;10:468. doi:10.3389/fendo.2019.00468.
36. Song CK, Jung SH, Kim D-D, Jeong K-S, Shin BC, Seong H. Disaccharide-modified liposomes and their in vitro intracellular uptake. *International Journal of Pharmaceutics*. 2009;380:161–9. doi:10.1016/j.ijpharm.2009.07.014.
37. Lei M, Ma G, Sha S, Wang X, Feng H, Zhu Y, Du X. Dual-functionalized liposome by co-delivery of paclitaxel with sorafenib for synergistic antitumor efficacy and reversion of multidrug resistance. *Drug Delivery*. 2019;26:262–72. doi:10.1080/10717544.2019.1580797.
38. Wang Y, Yang Y, Yu Y, Li J, Pan W, Yang X, Zhang Z, Jiang S, Yang X, Wang X. Transferrin Modified Dioscin Loaded PEGylated Liposomes: Characterization and In Vitro Antitumor Effect. *Journal of Nanoscience Nanotechnology*. 2020;20:1321–31. doi:10.1166/jnn.2020.16955.
39. Mohamed Kasim MS, Sundar S, Rengan R. Synthesis and structure of new binuclear ruthenium(II) arene benzil bis(benzoylhydrazone) complexes: Investigation on antiproliferative activity and apoptosis induction. *Inorganic Chemistry Frontiers*. 2018;5:585–96. doi:10.1039/c7qi00761b.
40. Mohamed Subarkhan MK, Ren L, Xie B, Chen C, Wang Y, Wang H. Novel tetranuclear ruthenium(II) arene complexes showing potent cytotoxic and antimetastatic activity as well as low toxicity in vivo. *European Journal of Medicinal Chemistry*. 2019;179:246–56. doi:https://doi.org/10.1016/j.ejmech.2019.06.061.
41. Mohamed Subarkhan MK, Ramesh R, Liu Y. Synthesis and molecular structure of arene ruthenium(ii) benzhydrazone complexes: impact of substitution at the chelating ligand and arene moiety on antiproliferative activity. *New Journal of Chemistry*. 2016;40:9813–23. doi:10.1039/C6NJ01936F.
42. Pang X-L, He G, Liu Y-B, Wang Y, Zhang B. Endoplasmic reticulum stress sensitizes human esophageal cancer cell to radiation. *World Journal of Gastroenterology*. 2013;19:1736–48. doi:10.3748/wjg.v19.i11.1736.
43. Ramalingam V, Revathidevi S, Shanmuganayagam T, Muthulakshmi L, Rajaram R. Biogenic gold nanoparticles induce cell cycle arrest through oxidative stress and sensitize mitochondrial

- membranes in A549 lung cancer cells. *RSC Advances*. 2016;6:20598–608. doi:10.1039/C5RA26781A.
44. Huang C, Sun Y, Shen M, Zhang X, Gao P, Duan Y. Altered Cell Cycle Arrest by Multifunctional Drug-Loaded Enzymatically-Triggered Nanoparticles. *ACS Applied Materials Interfaces*. 2016;8:1360–70. doi:10.1021/acsami.5b10241.
45. Allen-Petersen BL, Sears RC. Mission Possible: Advances in MYC Therapeutic Targeting in Cancer, *BioDrugs: Clinical Immunotherapeutics, Biopharmaceuticals and Gene Therapy*. 33 (2019) 539–553. doi:10.1007/s40259-019-00370-5.
46. Li M, Ning Y, Chen J, Duan X, Song N, Ding D, Su X, Yu Z. Proline Isomerization-Regulated Tumor Microenvironment-Adaptable Self-Assembly of Peptides for Enhanced Therapeutic Efficacy. *Nano Lett*. 2019. doi:10.1021/acs.nanolett.9b03136.
47. Scottà C, Fanelli G, Hoong SJ, Romano M, Lamperti EN, Sukthankar M, Guggino G, Fazekasova H, Ratnasothy K, Becker PD, Afzali B, Lechler RI, Lombardi G. Impact of immunosuppressive drugs on the therapeutic efficacy of ex vivo expanded human regulatory T cells. *Haematologica*. 2016;101:91–100. doi:10.3324/haematol.2015.128934.
48. Bharadwaj R, Sahu BP, Haloi J, Laloo D, Barooah P, Keppen C, Deka M, Medhi S. Combinatorial therapeutic approach for treatment of oral squamous cell carcinoma, *Artificial Cells, Nanomedicine, and Biotechnology*. 47 (2019) 572–585. doi:10.1080/21691401.2019.1573176.
49. Chen X, Wu W, Wang S, Zhong J, Djama NM, Wei G, Lai Y, Si X, Cao S, Liao W, Liao Y, Li H, Bin J. Magnetic Targeting Improves the Therapeutic Efficacy of Microbubble-Mediated Obstructive Thrombus Sonothrombolysis, *Thrombosis and Haemostasis*. (2019). doi:10.1055/s-0039-1695767.
50. Vakilinezhad MA, Amini A, Dara T, Alipour S. Methotrexate and Curcumin co-encapsulated PLGA nanoparticles as a potential breast cancer therapeutic system: In vitro and in vivo evaluation. *Colloids Surfaces B Biointerfaces*. 2019;184:110515. doi:10.1016/j.colsurfb.2019.110515.
51. Gies V, Zou S. Systematic toxicity investigation of graphene oxide: evaluation of assay selection, cell type, exposure period and flake size. *Toxicology Research*. 2018;7:93–101. doi:10.1039/c7tx00278e.
52. Bathla A, Rather RA, Poonia T, Pal B. Morphology Dependent Photocatalytic Activity of CuO/CuO-TiO₂ Nanocatalyst for Degradation of Methyl Orange Under Sunlight. *Journal of Nanoscience Nanotechnology*. 2020;20:3123–30. doi:10.1166/jnn.2020.17397.
53. Xu AY, Castellanos MM, Mattison K, Krueger S, Curtis JE. Studying Excipient Modulated Physical Stability and Viscosity of Monoclonal Antibody Formulations Using Small-Angle Scattering, *Molecular Pharmaceutics*. 16 (2019) 4319–4338. doi:10.1021/acs.molpharmaceut.9b00687.
54. Cui Z, Zhang X, Zhang X, He S, Gao W, He B, Wang X, Zhang H, Zhong Z, Zhang Q. Visualizing in vitro-in vivo correlation of miktoarm copolymer nanomicelles in cancer cellular uptake and trafficking, (2019). doi:10.1101/755595.
55. Chen Y, Liang Y, Jiang P, Li F, Yu B, Yan F. Lipid-PLGA hybrid microbubbles as a versatile platform for non-invasive image-guided targeted drug delivery. *ACS Appl Mater Interfaces*. 2019. doi:10.1021/acsami.9b10188.

56. Liu Y, Chen S, Sun J, Zhu S, Chen C, Xie W, Zheng J, Zhu Y, Xiao L, Hao L, Wang Z, Chang S. Folate-Targeted and Oxygen/Indocyanine Green-Loaded Lipid Nanoparticles for Dual-Mode Imaging and Photo-sonodynamic/Photothermal Therapy of Ovarian Cancer in Vitro and in Vivo. *Mol Pharm.* 2019;16:4104–20. doi:10.1021/acs.molpharmaceut.9b00339.
57. Yang H, Cai W, Lv W, Zhao P, Shen Y, Zhang L, Ma B, Yuan L, Duan Y, Yao K. A new strategy for accurate targeted diagnosis and treatment of cutaneous malignant melanoma: dual-mode phase-change lipid nanodroplets as ultrasound contrast agents. *International Journal of Nanomedicine.* 2019;14:7079–93. doi:10.2147/IJN.S207419.

Figures

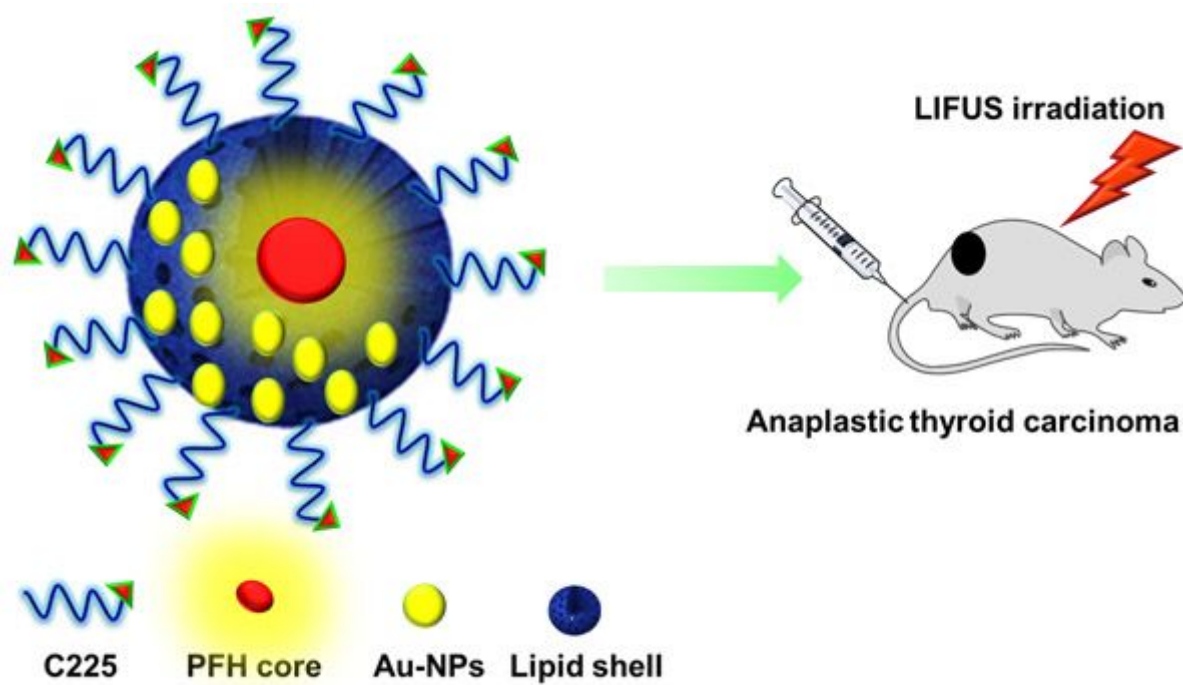


Figure 1

Design and NP formulation of C225 conjugates Au-PFH-NPs for safe and efficient in vivo drug delivery.

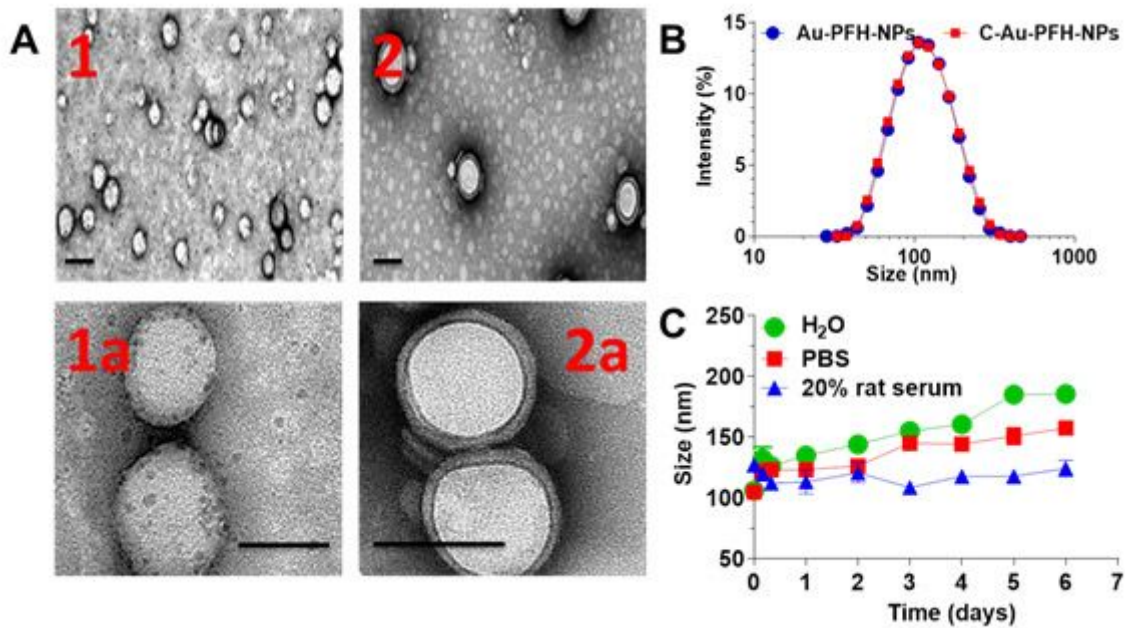


Figure 2

(A) TEM image of Au-PFH-NPs (1 and 1a zoom view) and C-Au-PFH-NPs (2 and 2a zoom view). Scale bars, 100 nm (B) DLS image of Au-PFH-NPs and C-Au-PFH-NPs. (C) Stability of Au-PFH-NPs and C-Au-PFH-NPs. in water with 50%, PBS and 20% rat serum at 37°C.

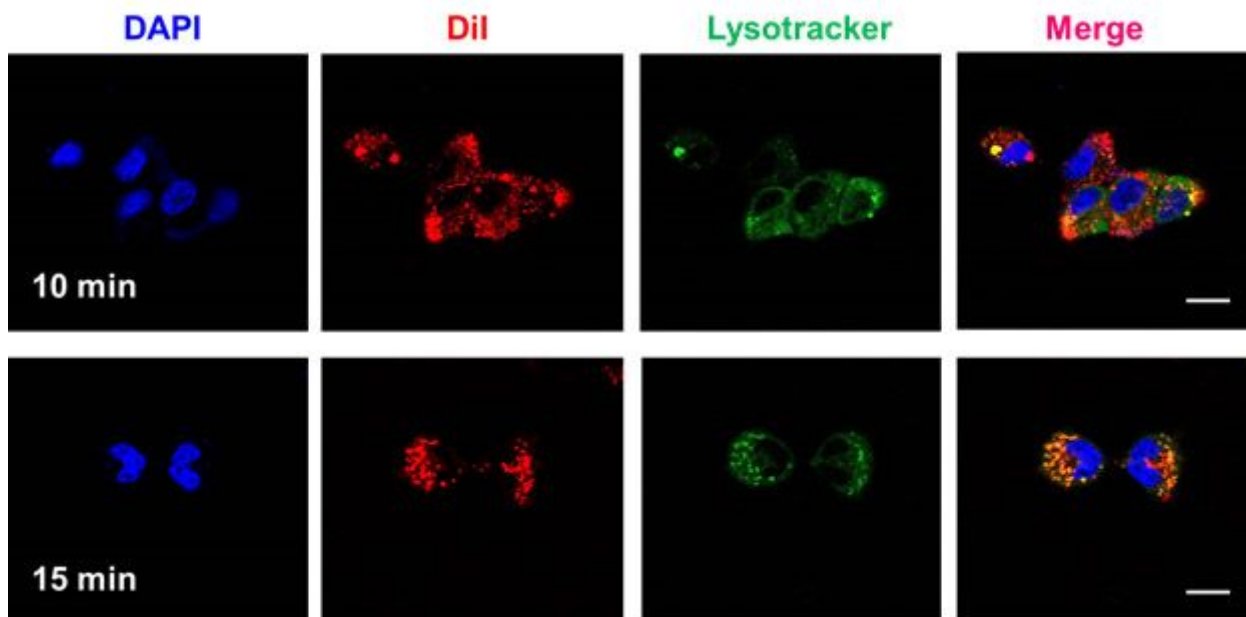


Figure 3

Cellular uptake of C-Au-PFH-NPs with 10 min and 15 minutes interval.

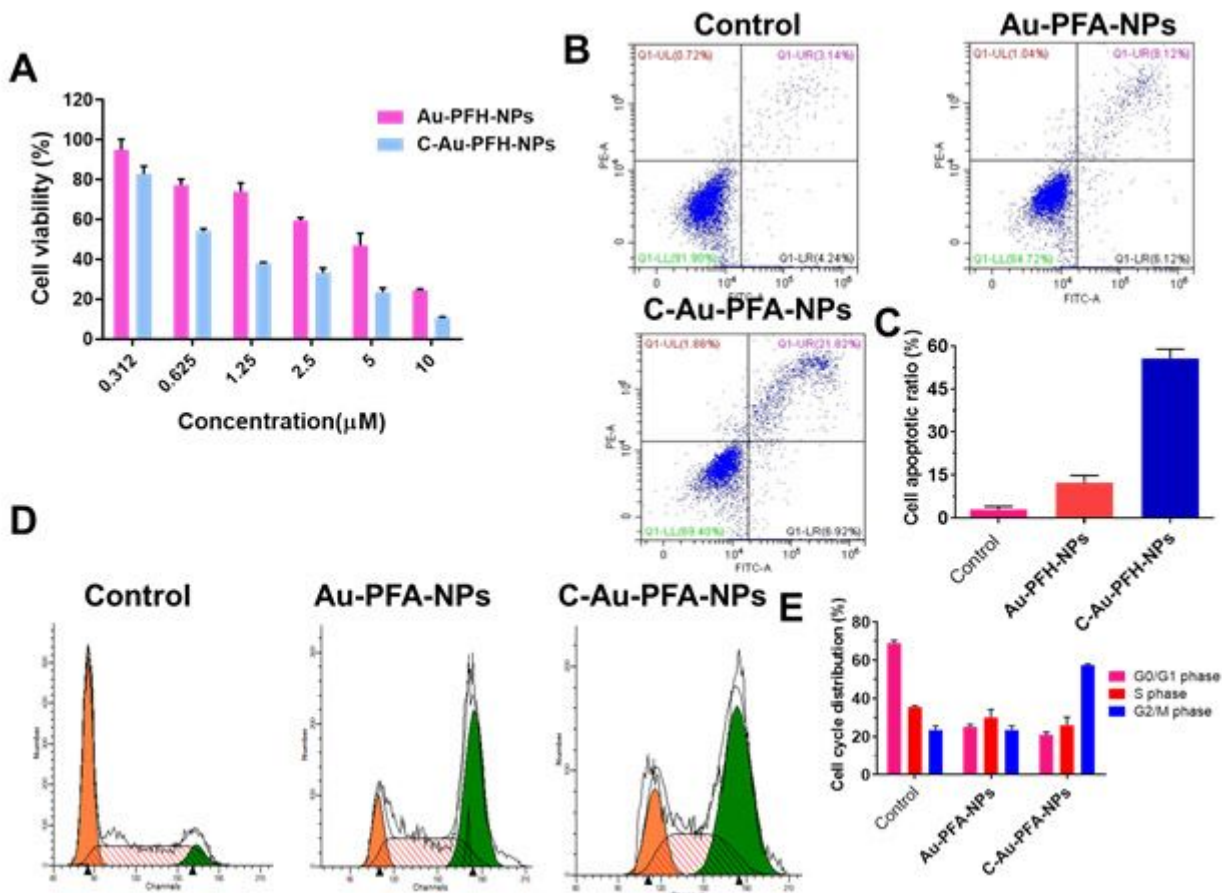


Figure 4

(A) In vitro cytotoxicity against C643 thyroid carcinoma cell. (B) Flow cytometry analysis of Au-PFH-NPs and C-Au-PFH-NPs. (C) Apoptosis quantification of flowcytometry analysis . (D) Cell cycle arrest of Au-PFH-NPs and C-Au-PFH-NPs. (E) quantification of cell cycle arrest.

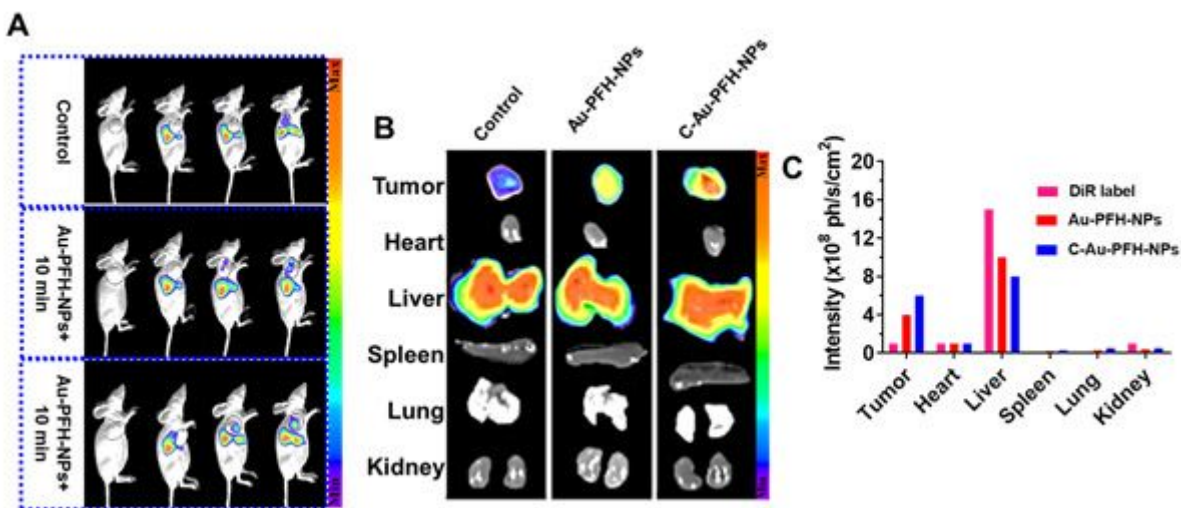


Figure 5

In vivo pharmacokinetics and biodistribution studies of Au-PFH-NPs and C-Au-PFH-NPs. (A) In vivo plasma of the drugs following intravenous injection of Au-PFH-NPs and C-Au-PFH-NPs. (B) The

biodistribution studies Au-PFH-NPs and C-Au-PFH-NPs. (C) The intensity of the DiR slabel Au-PFH-NPs and C-Au-PFH-NPs.

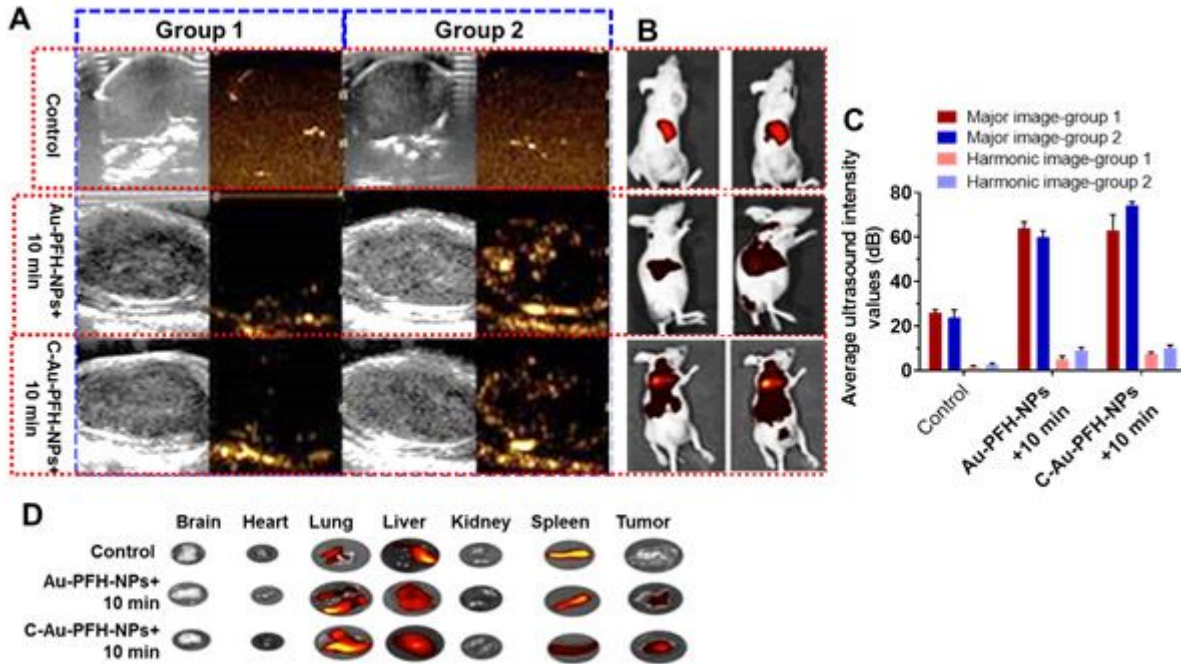


Figure 6

(A) Ultra sound image. (B) The organs used rats. (C) The average intensity values of Au-PFH-NPs and C-Au-PFH-NPs. (D) organs used ultra sound (Control-without ultra sound and Au-PFH-NPs and C-Au-PFH-NPs 10 minutes ultrasound exposure).

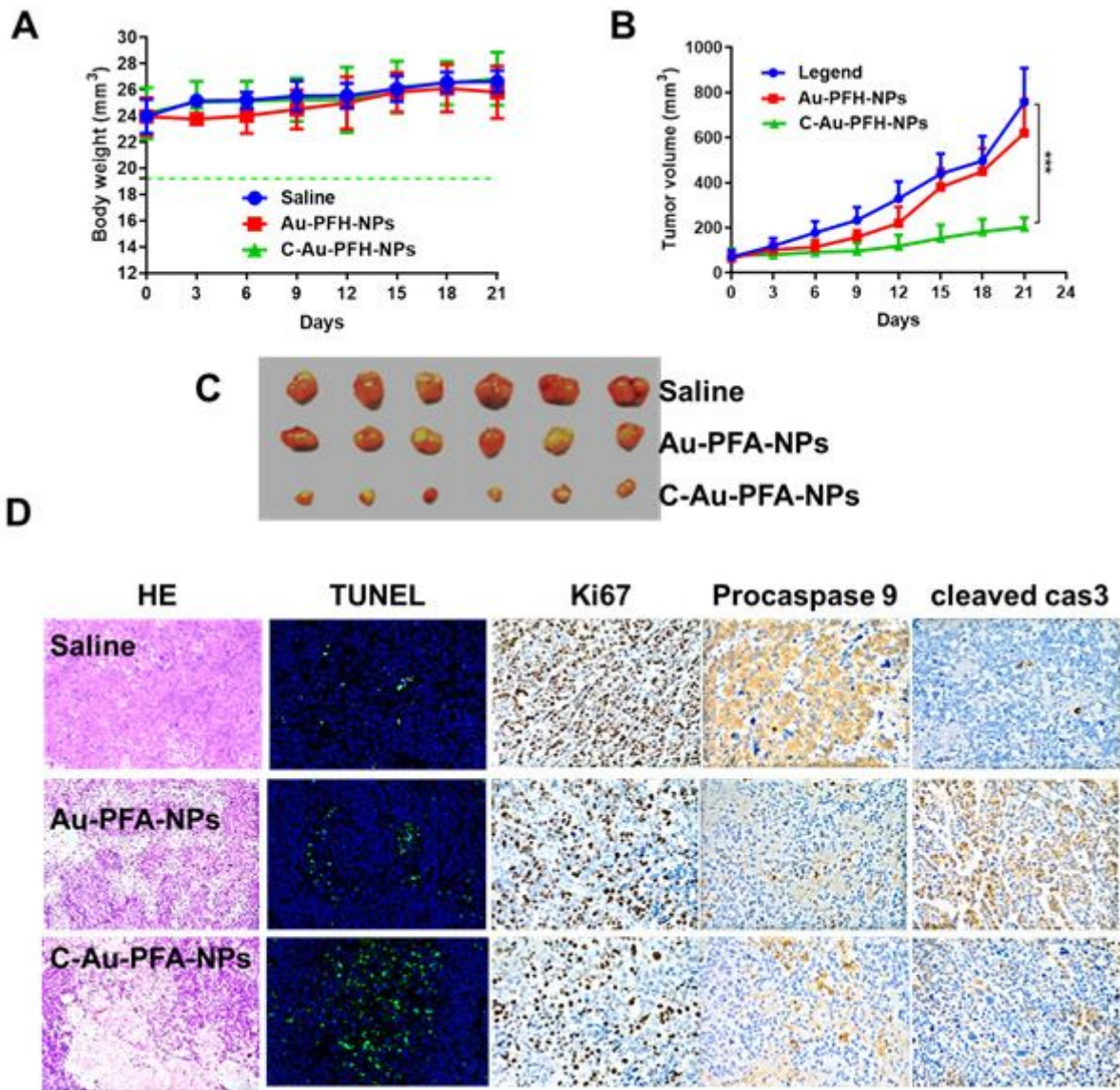


Figure 7

(A) Body weight, (B) Tumor volume (mm³). (C) Morphology of the tumors 21 days after treatment. The tumor volume, tumor weight and average body weight. (D) Representative HE, TUNEL, Ki67, procaspase, cleaved caspase 3 analysis of the excised tumors from the treated groups on post injection of the drugs. The image magnification is x400.